Undulator Linear Taper Control at the European X-Ray Free-Electron Laser

Sergey Tomin, Jan Kaiser, Nils Maris Lockmann,
Torsten Wohlenberg, Igor Zagorodnov
Deutsches Elektronen-Synchrotron DESY,
Notkestr. 85, 22607 Hamburg, Germany

(Dated: July 14, 2023)

Undulator tapering controls the resonance properties of the Free-Electron Laser (FEL) amplification process. Energy losses in an undulator, caused by synchrotron radiation and wakefields within the undulator's vacuum chamber, determine the undulator's linear taper. Synchrotron radiation contribution can be calculated analytically, while calculating wakefield energy loss necessitates a beam current profile.

We introduce a system for the automatic estimation of wakefield energy loss, which leverages non-invasive THz diagnostics, a current profile reconstruction algorithm enhanced with machine learning, and a recently developed analytical wakefield function for the undulator beamline. The effectiveness of this approach was validated by directly measuring wakefield-induced electron beam energy loss in the European XFEL's undulator section.

I. INTRODUCTION

In the pre-saturation exponential growth regime, the electron beam's energy loss due to FEL interaction is much smaller than ρ - FEL scaling parameter (known as the Pierce parameter). Thus, the energy exchange in this mode can be neglected, which allows us to use the uniform deflection parameter of the undulator K to maintain resonance. However, significant energy loss from spontaneous radiation emission, including higher harmonics (for $K > 1$), is occurring in long undulator beamlines, such as the European XFEL [1]. On the other hand, the electron beam interacts with the undulator vacuum chamber through wakefields, which result in beam energy losses that cannot be neglected either. To maintain the resonant condition in order to both not degrade the gain and maintain minimal SASE bandwidth [2], the undulator parameter K should be tapered as the beam energy decreases linearly with undulator distance.

The analytical formula for the energy loss of an electron beam in an undulator with length L and beam energy E due to spontaneous radiation is as follows:

$$U = \frac{4\pi^2}{3}\frac{r_e E^2 K^2 L}{mc^2 \lambda_w^2}. \tag{1}$$

where K is the undulator deflection parameter, λ_w the undulator period, r_e is classical radius of the electron. The contribution of the spontaneous radiation to the linear undulator taper can be easily calculated and is included in the undulator control system from the beginning of the European XFEL operation.

Calculating beam energy losses due to wakefields requires knowledge of both the impedance budget in the undulator beamline and the electron beam's current profile. To measure the current profile, we utilize an online non-invasive THz diagnostic called CRISP [4]. This diagnostic operates based on coherent diffraction radiation generated as the electron beam passes through an open aperture in the screen. The resulting THz spectrum is then processed using a reconstruction algorithm [6] to obtain the electron beam's current profile. However, the CRISP reconstruction has a few limitations. One limitation is its inability to distinguish between the head and tail of the beam, as it only measures the modulus of the Fourier transform of the current profile and not its phase [11]. Another limitation is of technical nature, as it is associated with limited temporal resolution when dealing with high peak currents and, conversely, a low signal-to-noise ratio for low current bunches [28]. These limitations can hinder the accurate estimation of wake losses of the lasing slice of the beam, especially when dealing with an asymmetrical current profile.

To overcome these limitations, we have developed a machine learning (ML) method that enables the reconstruction of a correctly oriented current profile, providing higher temporal resolution. Furthermore, we have established an analytical model for the undulator beamline's wake function [3], which is used to calculate wakefield energy loss. To validate the calculation of wakefield energy losses estimated with our approach, we conducted direct measurements. For this purpose, we utilized a calibration technique involving synchrotron radiation. This technique allows us to measure change in the beam energy, with reasonable accuracy, at the level of tens of MeV for a 14 GeV beam. As a result, we have confirmed that our approach can accurately estimate the total electron beam losses in the undulator, enabling linear taper control.

When setting up a European XFEL facility for photon delivery, a series of deterministic procedures are followed. These include BBA [12], emittance measurements, matching beam optics along the accelerator [13], and orbit correction, among others. However, in the final stage, a combination of automatic [15–17] and manual fine-tuning is often necessary to achieve optimal performance. The most commonly employed and effective parameters for fine-tuning include beam compression, orbit control within the undulator, phase shifter optimization, and both linear and nonlinear tapering of the undulator. With the introduction of this new system, we can now exclude the linear taper optimization from the overall optimization problem.

The paper is organized as follows: firstly, the undulator beamline geometry and its analytical wake function are described in Section II. Secondly, a brief description of the THz diagnostic CRISP and the reconstruction current profile method enhanced with ML is provided in Section III. Thirdly, the experimental validation of the wakefield energy losses calculation using a noninvasive diagnostic is presented in Section IV. Finally, the obtained results are discussed in Section V.

II. IMPEDANCE BUDGET OF THE UNDULATOR LINES

A. Impedance budget of the undulator cells

The European XFEL utilizes three long planar undulator lines: two hard X-ray undulators (SASE1/2) and one soft X-ray undulator (SASE3), Fig. 1. Each of these planar undulators consists of cells that adhere to a unified design. SASE1/2 contains 35 undulators with a period of 40 mm and SASE3 contains 21 undulators with a period of 68 mm.

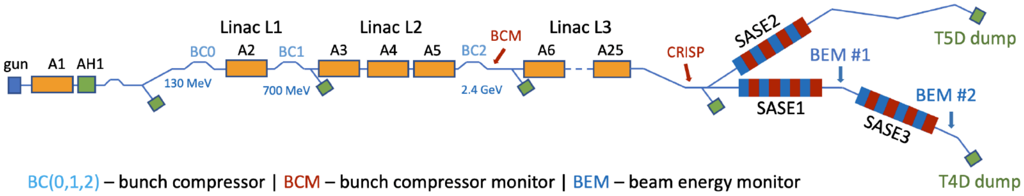

FIG. 1: Simplified layout of the European XFEL facility.

The individual cell contains a 5-meter long undulator and a 1.1-meter intersection, which houses components such as quadrupole, phase shifter, BPM, and various vacuum components. From the point of the wakefield calculation we have periodic structures with period $L = 6.1$ m of the same geometry for all three undulator lines. A detailed description of all the components of the undulator intersection, along with their contributions to the wakefield impedance, can be found in Appendix A.

An analytical approximation of the short-range longitudinal wake function of undulator periodic cells at the European X-ray Free Electron Laser was obtained in [3]. From numerical and analytical calculations the authors have found that the longitudinal wake function can be accurately approximated by the analytical expression

$$w_{\parallel}(s) = w_0(s) + \frac{\partial}{\partial s} w_1(s) + c\frac{R}{L}\delta(s), \tag{2}$$

$$w_0(s) = A\frac{Z_0 c}{\pi a^2}\exp\left(-\left(\frac{s}{s_0}\right)^{\alpha}\right)\cos\left(\frac{s}{s_1}\right), \tag{3}$$

$$w_1(s) = \frac{Z_0 c}{L\pi^2 a}\sqrt{2g_0 s}, \tag{4}$$

where $L = 6.1$ m, $A = 0.937$, $a = 5$ mm, $\alpha = 1.29$, $s_0 = 33.8$ μm, $s_1 = 9.86$ μm, $g_0 = 123$ mm, $R = 30.5\Omega$. The parameters are obtained by a numerical fit of the parametric form of function w_0 to the direct sum of the wakes of different elements listed in Table II Appendix A. Note that some of coefficients are different from those published in [3] as we have corrected an error in the estimation of the wake of the round pipe in the intersection. For a Gaussian bunch with charge of 250 pC compressed to the peak current of 5 kA the corrected impedance budget of one section with the contribution of all elements is shown in Table IV Appendix A.

The wake functions of different components of the undulator lines are calculated separately and the total wake function is obtained as a direct sum of the individual contributions. However, for the bunches much shorter than the pipe radius there must be significant impedance coupling between the components which are close to each other.

In order to investigate this question, we have created a rotationally symmetric model of the undulator vacuum chamber. The elliptical undulator pipe and other elements with the elliptical cross-section listed in Table II Appendix A have been replaced by round elements with an ”equivalent” radius [3]

$$a = \frac{g}{\sqrt{F_{\parallel}^{ellip}\left(\frac{g}{w}\right)}}, \qquad F_{\parallel}^{ellip}(x) = 0.279x^3 + 0.093x^2 + 0.013x + \pi^2/16,$$

where w is the half-width and g is the half-height of the elliptical cross-section. We have neglected the roughness and the oxide layer effects. Additionally we have considered only DC conductivity model. The pumping slots are replaced by round pipes of 5 mm radius.

For this ”round” model we have calculated the longitudinal wake function in the same way as described in paper [3]. The energy loss $U(z)$ due to this model increases uniformly along the undulator section and its change $\Delta U(\Delta z)$ relative to the beginning of the undulator section can be written as

$$\Delta U(\Delta z) = ek_{\|}\Delta z,$$

where Δz is the position in the undulator section relative to the beginning of the section, e is the charge of electron, $k_{\|}$ is the ”analytical” loss factor (per meter).

Alternatively, we have done direct numerical calculations with time-domain code ECHO [27]. Here we have started from the perfectly conducting pipe and considered 3 undulator sections with the total length of 18.3 m. The Gaussian bunch is traveling on the axis and we have calculated the energy loss of the bunch along the undulator line:

$$U(z) = -e\int_{-\infty}^{\infty} W_{\|}(s,z)\lambda(s)ds, \quad W_{\|}(s,z) = -\frac{1}{Q}\int_{-\infty}^{z-s} E_z\left(z', t = \frac{z'+s}{c}\right)dz'.$$

The comparison of the ”analytical” energy loss with the one obtained from the numerical calculations is shown in Fig. 2. The left plot shows the results for the rms bunch length σ of 50 μm. The solid black line presents the grow of the energy loss along one middle undulator section. The dotted black line describes the energy loss grow in the first undulator section. The curves are different due to transitive effects at the beginning of the undulator line. The gray dashed curve presents the ”analytical” energy loss. The similar results for the much shorter bunch length of 10 μm are shown at the right plot of Fig. 2.

If we define the ”interference” factor $F_{int}(\sigma)$ as a ratio of the numerical energy loss at the end of middle section to the ”analytical” energy loss of one section then we can write $F_{int}(50\ \mu m) = 0.84$, $F_{int}(10\ \mu m) = 0.91$. Such behavior of the

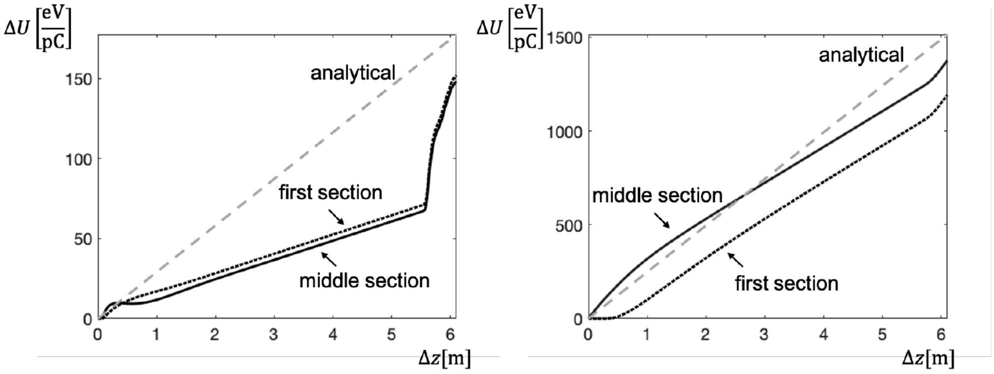

FIG. 2: The comparison of the ”analytical” energy loss with the energy loss obtained from the numerical calculations with code ECHO for rotationally symmetric geometry. The left plot shows the results for the bunch length of 50 μm. The right plot shows the results for the bunch length of 10 μm. The solid black lines present the grow of the energy loss along one middle undulator section. The dotted black lines describe the energy loss grow in the first undulator section. The gray dashed lines present the ”analytical” energy loss.

interference factor can be explained by smaller contribution of ”geometrical” wake relative to the contribution of the resistive wake for the shorter bunch length.

For the Gaussian bunch of length $\sigma = 10\ \mu$m the catch-up distance in the pipe of radius $a = 5$ mm can be estimated as $\sigma^2/a = 2.5$ m. Indeed, we see at the right plot of Fig. 2 that the black solid curve demonstrates the steady-state behavior only after 2 meters from the beginning of the elliptical pipe.

From the analysis of the transitive behavior we can conclude that the analytical model, Eq.(2), could overestimate the total loss factor. However, for Gaussian bunches shorter than $10\,\mu$m the overestimation is below 10%.

B. Wakefields of the experiment in undulator line SASE3

The measurement of the energy loss was done in the SASE3 undulator line between two BEMs (beam energy monitor) separated by 474 meters as shown in Fig. 1.

Impedance budget or the vacuum section between two BEMs consists of four main parts: (1) 23 standard undulator cells, (2) chicane cell, (3) 4 cells for the helical undulators and (4) round vacuum chamber of radius 20.25 mm with length of 318 m, illustrated in Fig. 3. In the chicane cell the elliptical pipe is replaced by a flat pipe with the old elliptical shape at one end and round shape at another end. The bunches without deflection see approximately the same wakefields as in the standard undulator cell. Hence we included this cell in the impedance budget as the standard undulator cell.

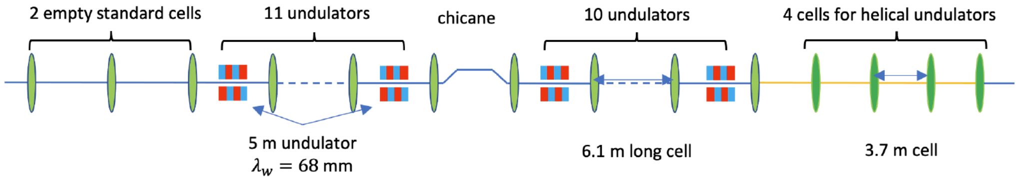

FIG. 3: SASE3 undulator line layout.

To estimate the wake function for the helical cells we followed the same approach as in [3]. The length of the intersection is 0.7 m. At the moment of the experiment in March 2021 the undulator pipe of 3 m was yet not installed and presented by standard stainless steel pipe of large radius of 20.25 mm. The contribution of several step-outs from radius of 5 mm to radius of 20.25 mm was estimated numerically by ECHO in order to take into account the transitive effects.

In order to show relative contribution of these three main parts to the total wake we considered a short Gaussian bunch with rms length of 6 μm and charge of

250 pC. Figure 4 shows the wakes of the different parts. As expected the main contribution is done by the undulator cells.

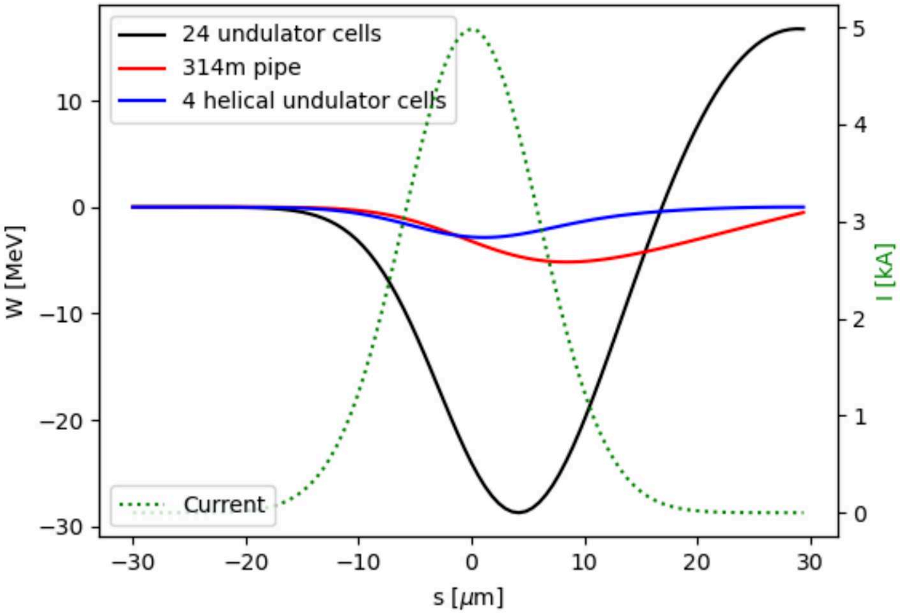

FIG. 4: The wakes of different parts for the Gaussian bunch with length of 6 μm.

III. BEAM CURRENT PROFILE RECONSTRUCTION

A direct measurement of the current profile in the time domain can be achieved using transverse deflecting structures (TDS). These structures facilitate the mapping of the longitudinal bunch distribution onto a transverse plane, enabling the observation and visualization of the current profile on a view screen [22]. However, measurements using TDS are invasive and constrained by the damage thresholds of view screens and the radiation limits for the emission of secondary particles. These limitations restrict the practicality and feasibility of conducting extensive or high-repetition-rate measurements using this method.

A complementary approach to monitor the current profile is based on spectroscopy of coherent radiation emitted by the electron bunch. The coherent radiation spectrum and current profile of the electron bunch are linked via Fourier transform [23]. At the European XFEL, coherent diffraction radiation (CDR) is generated by the electron bunch passing through an aperture inside an aluminum screen just upstream of the kicker-septum distribution system (see Fig. 1). While the electron bunches proceed undisturbed to the SASE beamlines, the THz and infrared spectrum of the CDR is detected by a multistage grating spectrometer called CRISP [5]. CRISP at the European XFEL is operated at the megahertz electron bunch repetition rates and due to CDR as radiation source a noninvasive current profile diagnostic [4].

Spectroscopic measurements are missing the phase function of the Fourier transform of the current profile which would be required for a direct identification. Instead, the phase function is obtained based on a combination of analytical and iterative phase retrieval methods as described in [6]. This approach, referred to as CRISP reconstruction, has demonstrated by comparative TDS measurements to perform excellently [4]. It is worth noting that, due to the missing phase function head and tail of the beam cannot be distinguished [11]. While this limitation does not pose a problem for operation or compression setups, it can impede the accurate estimation of wake losses in the lasing beam core if its position within the bunch is known, especially when dealing with an asymmetrical current profile.

To address this, we have developed a machine learning (ML) method to infer a correctly oriented current profile by incorporating two inputs: a 5-dimensional vector of RF settings $x_{\mathrm{RF}} = (\alpha, \rho, \psi, \alpha_{\mathrm{L1}}, \alpha_{\mathrm{L2}})$ and the 240-dimensional THz form factor vector x_{THz} sampled from the range of 0.7 to 58 THz [25]. The RF settings α, ρ, ψ are translated to Injector chirp, curvature, and skewness, while $\alpha_{\mathrm{L1}}, \alpha_{\mathrm{L2}}$ correspond to Linac L1 and Linac L2 chirps, respectively. The energy gain of the electron beam for these three stages is defined by design and can be found in Fig. 1. Both these inputs are concatenated and then passed through a multilayer perceptron (MLP) neural network model, which then outputs 300 ordered samples of the current profile. The neural network is trained in a supervised setup to infer current profiles closely resembling those generated by a start-to-end beam dynamics simulation. The start-to-end beam dynamics simulations were performed using the OCELOT simulation code [8]. The tracking was conducted with 40k particles, including collective effects, following a similar approach as described in [9]. We conducted 32000 simulations on the DESY high-performance cluster, randomly scanning RF parameters, which correspond to different beam compressions. From the current profiles $_I$ obtained from the simulations, we generated CRISP form factors using the FFT algorithm and applied a CRISP spectrometer apparatus function that also models signal noise.

One of the difficulties in developing this neural network model is that the model must predict the current profile of bunches whose length can vary by a factor of 10 (Fig. 6), with acceptable resolution of the order of femtoseconds.

In order to cover a long bunch, the samples must be spread out over a wide range. In order to cover short bunches with adequate resolution, one must have a large number of samples. Not only does this needlessly increase the size of the neural network model, it also means that a lot of the time, most of the neural network outputs are not predicting any useful information. This can lead to the model learning to output 0.0 on these simply because this is correct most of the time, instead of even attempting to learn the correct function for that particular sample.

We solve this problem by adding the bunch length $\hat{y}_s$ from the first to the last current sample as a second output of the neural network model. The 300 samples are then equidistantly arranged over the bunch length that the model inferred. This way, an adaptive resolution of the current profile $\hat{y}_I$ reconstructed by our model automatically reveals all relevant features, while also ensuring that the entire bunch is captured. The resulting neural network model $\mathcal{M}$ is given as

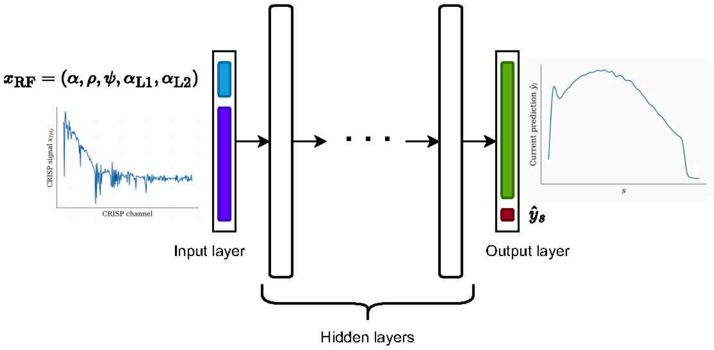

FIG. 5: Flowchart of the neural network architecture used for reconstructing the current profile. On the left side, the neural network receives input in the form of RF settings and THz spectrum. The signal is then passed through multiple hidden layers, and ultimately the current profile and bunch length are output on the right-hand side.

$$\hat{y}_I, \hat{y}_s = \mathcal{M}(x_{\mathrm{RF}}, x_{\mathrm{THz}})$$

In between the input and the output layer, there are from 2 to 6 hidden layers, as is illustrated in Fig. 5. Each hidden layer may be followed by batch normalisation before the activation. The outputs use a different activation from hidden layers. Namely, a *Softplus* activation is chosen as the output activation function. The latter ensures that all outputs are strictly positive, as they physically should be, while also ensuring that there remains some gradient when the output should be zero according to the ground truth. If a *rectified linear unit (ReLU)* activation function were used on this output, gradients may be lost when 0 is output, which results in fully trained models that have single 0 samples where they stopped learning. We use a *mean squared error (MSE)* loss function L over each output where both outputs are weighted the same as in

$$L(y, \hat{y}) = \mathrm{MSE}(y_s, \hat{y}_s) + \mathrm{MSE}(y_I, \hat{y}_I)$$

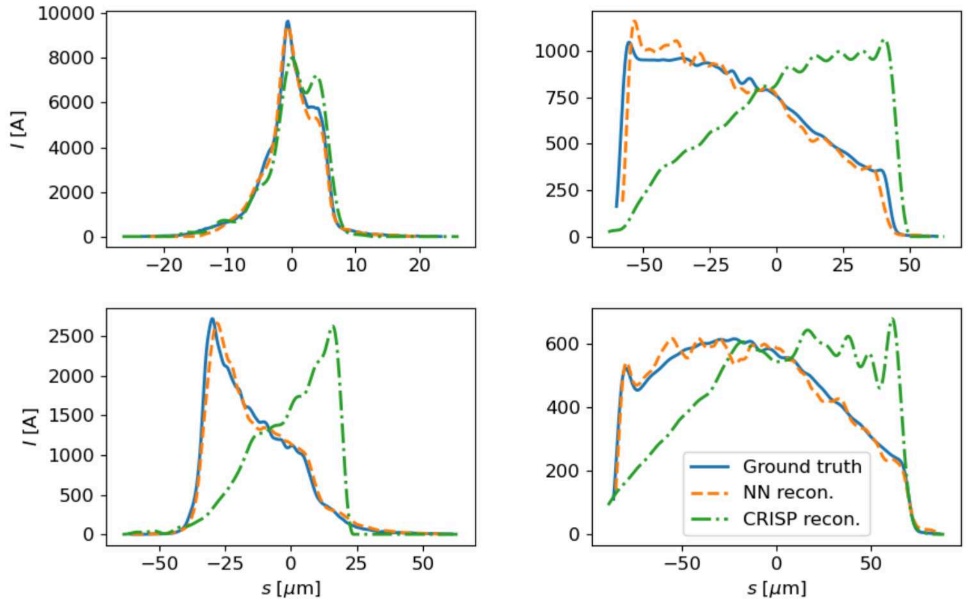

FIG. 6: Comparison of ground truth, ML and CRISP reconstructed current profiles for random samples from the hold-out dataset.

with

$$\mathrm{MSE}\,(y, \hat{y}) = \frac{1}{n}\sum_{i=0}^{n}(y_i - \hat{y}_i)^2$$

For training, an *Adam* [26] optimiser is used with $\beta_1 = 0.9$ and $\beta_2 = 0.999$. Hyperparameters such as the number and width of hidden layers, or the learning rate were tuned using Bayesian optimisation to minimise the loss over the validation dataset. The final used hyperparameters for 1-dimensional current reconstruction are listed in Table I. The training dataset obtained from the simulations was randomly split into training, validation and test sets according to the ratios $(80\,\%, 10\,\%, 10\,\%)$. The RF settings and formfactors are normalised over the training dataset to follow a standard normal distribution. Current profiles and bunch lengths are normalised to a range of $(0, 1)$.

TABLE I: Hyperparameters used during training of the reconstruction model

Parameter name	**Value**
# Hidden layers	3
Hidden layer width	267
Hidden activation	ReLU
Batch normalisation	Yes
# Training epochs	76
Learning rate	0.003
Batch size	66

In Fig. 6, four randomly selected examples are shown, each displaying the ground truth (current profile from the simulation dataset) as well as its reconstruction using the NN and CRISP methods. As can be seen, there is good agreement between the ground truth and the profiles inferred by our neural network model in all four cases. In the case of the CRISP reconstruction, we observed that some of the current profiles are inverted, but the overall reconstructed current shape is in good agreement with the ground truth. It is worth noting that for samples A and D in Fig. 6, the CRISP reconstruction does not perform as well as the NN, because it is only based on CRISP and does not take RF parameters into account. In the case of high current, the time resolution of CRISP, which is about 8 fs [28], becomes a limiting factor, while for low current (< 1 kA), the low signal level of CRISP limits the reconstruction performance.

Let's examine Fig. 6**C** more closely and estimate average energy loss of the particle in the beam, also known as the loss factor, in the undulator vacuum chamber for the current profiles obtained with NN and CRISP reconstructions. The peculiarity of these profiles is that they are similar to each other but inverted. The loss factor can be calculated using the following formula:

$$< W(s) > = \int_{-\infty}^{\infty} W(s)\lambda(s)ds \tag{5}$$

$$W(s) = \int_{0}^{\infty} w_{||}(s')\lambda(s-s')ds' \tag{6}$$

where $W(s)$ is wake potential, and $w_{||}$ wake function Eq. (2).

The loss factor does not depend on the orientation of the current profile. This can be easily demonstrated by substituting one formula into another and changing the order of integration.

$$< W(s) > = \int_{-\infty}^{\infty}\int_{0}^{\infty} w_{||}(s')\lambda(s-s')\lambda(s)ds'ds = \tag{7}$$

$$= \int_{0}^{\infty} ds' w_{||}(s') \int_{-\infty}^{\infty} \lambda(s)\lambda(s-s')ds' \tag{8}$$

where $\int_{-\infty}^{\infty} \lambda(s)\lambda(s-s')ds'$ is the autocorrelation function of the current profile, which exhibits symmetry.

The loss factor for both cases, as expected, is similar and equal to approximately 48 keV/m. Now, let's consider that we know the position of the lasing slice, which corresponds to the center of mass of the beam. When we calculate the energy loss for the center of mass, we obtain different values. The NN reconstruction yields an energy loss of approximately 75 keV/m, whereas for CRISP reconstruction, it is only 53 keV/m (see Fig. 7). However, if the lasing slice corresponds to the maximum current amplitude, the wakefield losses for both NN and CRISP reconstructions are similar, with values of approximately 73 keV/m and 68 keV/m, respectively.

IV. EXPERIMENTAL VALIDATION OF THE WAKEFIELD ENERGY LOSSES

Wakefield energy losses were measured in the SASE3 undulator line. The SASE undulator was selected for two reasons. Firstly, it provided conveniently located

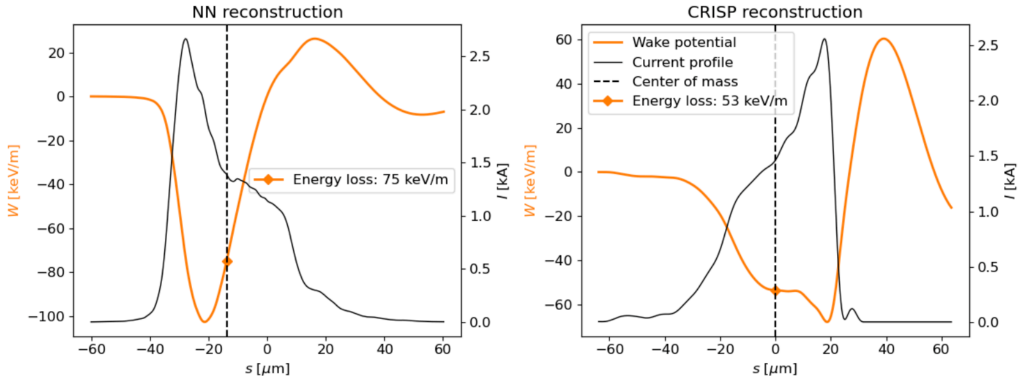

FIG. 7: Current profiles and wake potentials for the case Fig. 6C. Left: NN reconstruction current profile and wake potential, right: CRISP reconstruction.

diagnostics for electron beam energy measurements, known as the beam energy monitors (BEMs), as shown in Fig. 1. Secondly, the vacuum chamber between the BEMs was relatively simple, which facilitated the theoretical estimation of the impedance budget.

A. Calibration of the beam energy measurement diagnostics

Beam energy monitors (BEMs) are capable of measuring the absolute energy of an electron beam with an accuracy of about 1%, which is insufficient for directly measuring beam energy changes in the 10-20 MeV range caused by wakefield energy losses. To overcome this limitation, we proposed a method for calibrating the BEM using the beam energy loss due to spontaneous emission. In Fig.3, it can be seen that SASE3 is comprised of 21 undulators, each 5 m long with a period of 68 mm. These undulators were sequentially closed in groups of three cells to a minimum gap corresponding to 660 eV at a beam energy of 14.1 GeV. The resulting beam energy changes were recorded by BEM #2, as shown in Fig.8. The theoretical prediction given by Eq. 1 is also displayed in the figure, indicating that the raw measurements of BEM #2 overestimate the actual losses by a factor of 1.99/1.28. A similar technique was recently employed in [10], demonstrating good agreement with direct measurements.

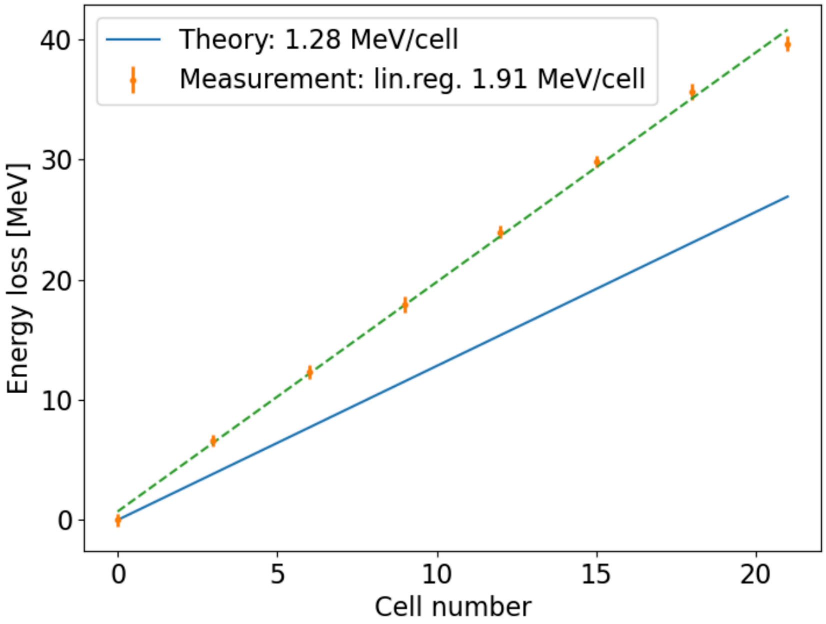

FIG. 8: Measurements of the energy loss due to spontaneous radiation and linear regression of the measurement points. Blue line is energy losses according to theoretical prediction.

While performing compression scans, it is reasonable to expect beam energy changes at the position of BEM #1, resulting from wakefields in the vacuum chamber of the accelerator segment from linac L1 to BEM #1. Rather than applying the same calibration procedure to the first BEM, we maintained a constant beam energy throughout the entire experiment at this position, using energy FB based on the last RF station A25. This approach simplifies the experimental data analysis.

B. Measurements results

The experiment was conducted as follows. We scanned the linac L1 chirp from +6 to -12 m^{-1}. The chirp is defined as $chirp = \frac{-kVsin(\phi)}{E_0+Vcos\phi}$, where V and ϕ are the voltage and phase of linac L1, $E_0 = 130$ MeV is the initial energy of the beam before L1, and $k = 2\pi f/c$, $f = 1.3$ GHz. Such a wide range was chosen to pass through the full compression. That is initially low compression and, accordingly, a low beam current amplitude at a positive chirp. As the chirp changed towards negative values, the compression increased, reaching its maximum at a chirp value of -8.5 m^{-1}. After passing through full compression, the overcompression phase began, and the current amplitude started to decrease. The scanning step was chosen to be non-uniform, with a denser grid around the region of full compression. The scan was carried out twice, with the laser heater (LH) [30] turned off and on. The laser heater introduces an uncorrelated energy spread, which results in a reduced current amplitude at full compression. The laser heater's intensity was selected to be near its maximum capacity, ensuring that its impact would be clearly visible. The final beam compression was also independently monitored by the beam compression monitor (BCM) [24] after last bunch compressor BC2, Fig. 1. Accordingly, we expected to see two similar curves with different amplitudes from the BCM. The curve with the smaller amplitude corresponds to scanning with the laser heater on, which corresponds to lower compression as expected, Fig. 9.

At each scanning step, we acquired the coherent diffraction radiation spectrum of the electron beam using CRISP for subsequent beam current profile reconstruction. We measured the energy loss of the entire bunch, also known as the loss factor, which depends solely on the shape of the current profile and not on its orientation. In this particular case, we utilized CRISP reconstruction as not all RF parameters for NN reconstruction were reliably recorded during the time of the experiment in March 2021.

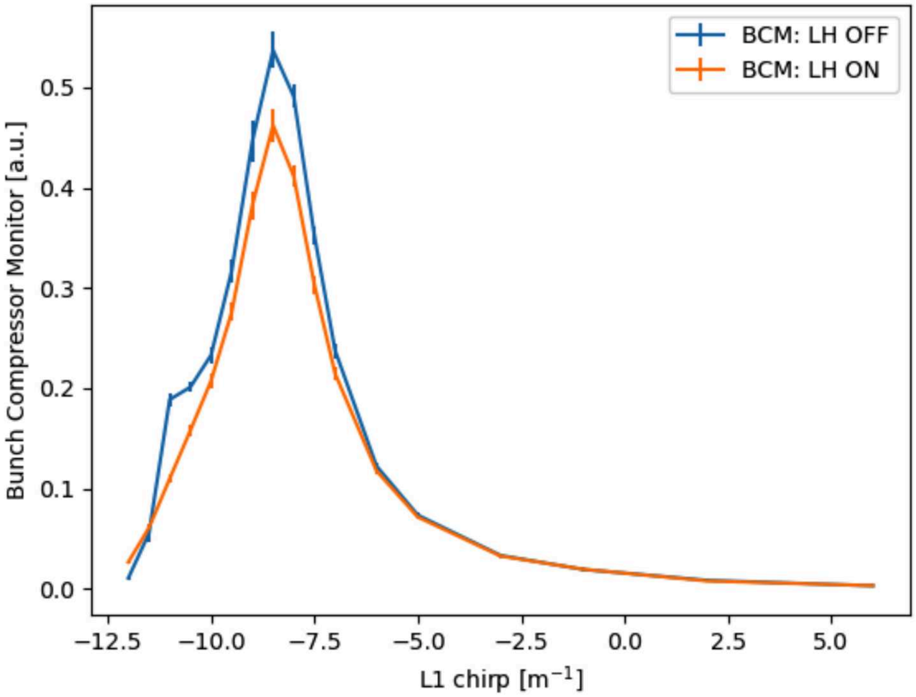

FIG. 9: Signal from Bunch Compressor Monitor after the last bunch compressor BC2.

The measurement of the beam energy loss due to wakefields was carried out using BEM #2 and a previously measured calibration coefficient $C = 1.28/1.99$. As mentioned earlier, the electron beam energy at the BEM #1 position remained constant due to energy feedback.

These measurements of beam energy loss are relative, as we assumed zero energy loss at the lowest compression (chirp = +6 m^{-1}). This assumption was made based on the estimation that the current profile amplitude was on the order of 0.1 kA at the lowest compression point (chirp = +6 m^{-1}), resulting in wakefield energy losses in the range of 0.3-0.4 MeV. However, CRISP cannot reliably reconstruct current profiles below 1 kA due to a low signal-to-noise ratio, as mentioned earlier. As a result, only a portion of the scan, specifically from -12 to -2.5 m^{-1}, can be utilized for the analytical estimation of wakefield energy losses. The final results, as depicted in Fig. 10, demonstrate a reasonable agreement between the analytical estimation based on CRISP reconstruction and direct measurements.

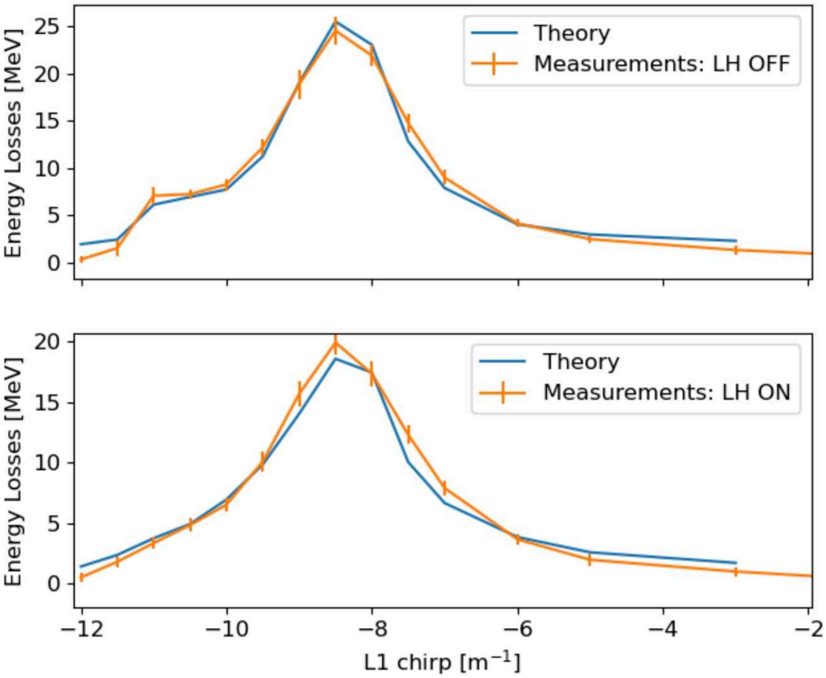

FIG. 10: Comparison between direct measurements of the energy loss and analytical estimations.

V. DISCUSSION

Wakefield energy losses in the undulator section can have a greater impact on determining the linear undulator taper compared to synchrotron radiation losses. This can be observed in Fig. 11, which depicts the dependence of electron beam energy losses for 14 GeV beam in SASE1 undulator due to synchrotron radiation as a function of photon energy. The horizontal lines in the figure indicate wakefield energy losses for the center of mass of a Gaussian beam with current amplitudes of 3 kA, 5 kA, and 7 kA.

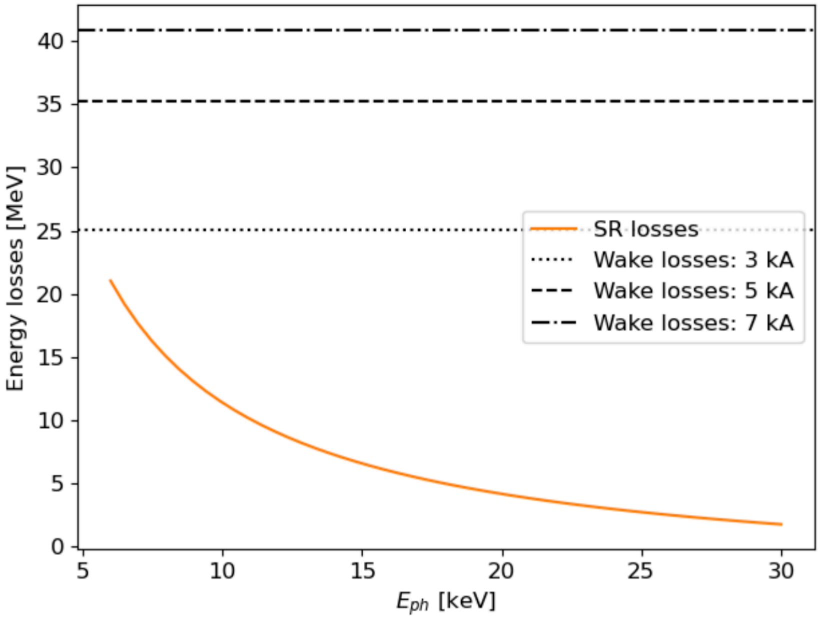

FIG. 11: Beam energy losses due to synchrotron radiation in SASE1 undulator (35 cells) as a function of undulator photon energy and wakefield energy losses of the beam core for Gaussian beams with amplitudes of 3 kA, 5 kA, and 7 kA. Electron beam energy 14 GeV.

Despite this fact, at the European XFEL, only synchrotron radiation (SR) energy losses are automatically taken into account for the linear taper. The contribution of wakefield losses to the linear taper is optimized through manual tuning.

In this study, we have shown and experimentally proven that the available noninvasive diagnostic at European XFEL, along with the theoretically calculated impedance budget of the undulator vacuum chamber, is sufficient to predict wakefield energy losses with reasonable accuracy.

An open question remains regarding how to define the lasing slice for a better estimation of the linear taper. One potential solution is the utilization of the recently installed diagnostics dechirper [29]. However, it should be noted that the LPS diagnostics is installed after the SASE2 undulator and cannot be used during photon delivery.

Additionally, we are looking forward to utilizing LPS virtual diagnostics [25, 31] that can be used in the control room. While this is still a question for the future, in the meantime, we propose compensating wakefield losses for the slice corresponding to the highest amplitude of the current profile.

By incorporating these advancements, we can automatically predict the linear taper, potentially enhancing lasing performance and reducing the dimensionality of the FEL tuning optimization problem.

Appendix A: Impedance budget of undulator cell

The individual undulator cell contains a 5-meter long undulator and a 1.1-meter intersection. The list of all the components that contribute to the wake potentials is shown in Table II. The properties of the materials used in the estimation of the steady-state resistive wall wakefields are presented in TableIII.

For the Gaussian bunch with charge of 250 pC compressed to the peak current of 5 kA the impedance budget of one section with the contribution of all elements is shown in Table IV.

---

[1] W. Decking, S. Abeghyan, P. Abramian, A. Abramsky, A. Aguirre, C. Albrecht, P. Alou, M. Altarelli, P. Altmann, K. Amyan, V. Anashin, E. Apostolov, K. Appel, D. Auguste, V. Ayvazyan, S. Baark, F. Babies, N. Baboi, P. Bak, V. Balandin et al., A MHz-repetition-rate hard x-ray free-electron laser driven by a superconducting linear

TABLE II: The components of the undulator lines along one section of length of 6.1 m.

N	Name	Half-width mm	Half-height mm	Position mm	Length mm	Material
1	Elliptical gasket	7.525	4.425	0	0.5	Silver
2	Flange, type I	7.5	4.4	0.5	13.0	Steel 316LN
3	Flange, type II	7.5	4.4	13.5	12.55	Aluminum
4	Weldseam	8.1	5	26.05	0.1	Steel 316LN
5	Elliptical pipe	7.5	4.4	26.15	5436.7	Aluminum
6	Weldseam	8.1	5	5462.85	0.1	Steel 316LN
7	Flange, type II	7.5	4.4	5462.95	12.55	Aluminum
8	Flange, type I	7.5	4.4	5475.5	13.0	Steel 316LN
9	Elliptical gasket	7.525	4.425	5488.5	0.5	Silver
10	Flange, type III	7.5	4.4	5489	27.5	Copper
11	Absorber	4.5	4	5516.5	3	Copper
12	Round pipe	5	-	5519.5	22.2	Copper
13	Below gap	12.75	-	5541.7	2.5	Copper
14	Round pipe	5	-	5544.2	96.3	Copper
15	Pumping slots	5	-	5640.5	21	Copper
16	Round pipe	5	-	5661.5	48.5	Copper
17	Round gasket	5.025	-	5710	0.5	Silver
18	BPM	5	-	5710.5	99	Steel 316LN
19	Round gasket	5.025	-	5809.5	0.5	Silver
20	Round pipe	5	-	5810	68.5	Cooper
21	Below gap	12.75	-	5878.5	2.5	Copper
22	Round pipe	5	-	5881	211	Copper
23	Round/elliptical transition	5 to 7	5 to 4.4	6092	8	Copper

TABLE III: Material properties.

Material	Conductivity $(\Omega m)^{-1}$	Relaxation time fs	Oxide layer nm	Roughness nm
Aluminum	$3.66 \cdot 10^7$	7.1	5	300
Copper	$5.8 \cdot 10^7$	24.6	5	300
Steel 316LN	$1.4 \cdot 10^6$	2.4	0	300
Silver	$6.2 \cdot 10^7$	40	0	300

TABLE IV: Impedance budget of one undulator section with length of 6.1 m for the Gaussian bunch with charge of 250 pC compressed to the peak current of 5 kA

N	Name	Positions	Total length mm	Loss kV	Spread kV
1	Elliptical pipe	5	5426.7	584.0	275.5
2	Round pipe	12, 14, 16, 20, 22	446.5	49.5	24.0
3	Absorber	11	3.0	71.2	28.0
4	Round/elliptical transition	23	8.0	37.1	14.6
5	BPM	18	99.0	28.7	13.4
6	Below gaps	13, 21	5.0	12.0	4.8
7	Elliptical gaskets	1, 9	1.0	5.1	2.1
8	Round gaskets	17, 19	1.0	5.4	2.2
9	Pumping slots	15	21.0	5.3	2.2
10	Flanges, type I	2, 8	26.0	3.8	2.1
11	Flanges, type II	3, 7	25.1	2.7	1.3
12	Flange, type III	10	27.5	3.0	1.4
13	Weldseams	4, 6	0.2	2.3	0.9
	Totally		6100	811.4	352.5

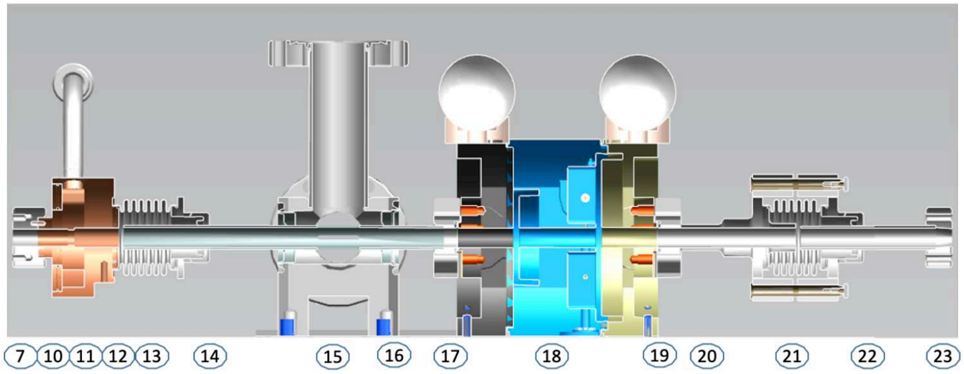

FIG. 12: The layout of the undulator intersection. The numbers under the elements correspond to the positions in Appendix V in Table II.

accelerator, Nat. Photonics 14, 391 (2020).

[2] W. M. Fawley et al.,"Tapered undulators for SASE FELs", Nucl. Instrum. Methods A, vol. 483, pp. 537-541, 2002. doi: 10.1016/S0168- 9002(02)00377- 7

[3] I.Zagorodnov et al., Short-range longitudinal wake function of undulator lines at the European X-ray free electron laser, Nucl. Instrum. Methods A, vol. 1043, 2022, 167490, https://doi.org/10.1016/j.nima.2022.167490

[4] Lockmann NM, Gerth C, Schmidt B, Wesch S., Noninvasive Thz Spectroscopy for bunch Current Profile Reconstructions at Mhz Repetition Rates. Phys Rev Accel Beams (2020) 23:112801. doi:10.1103/PhysRevAccelBeams.23.112801

[5] S.Wesch, B. Schmidt, C. Behrens, H. Delsim-Hashemi, P. Schmüser, A multi-channel THz and infrared spectrometer for femtosecond electron bunch diagnostics by single-shot spectroscopy of coherent radiation, Nucl. Instrum. Methods Phys. Res., Sect. A 665 40 (2011).

[6] B. Schmidt, N. M. Lockmann, P. Schmüser, and S. Wesch, Benchmarking Coherent radiation spectroscopy as a tool for high-resolution bunch shape reconstruction at free-electron lasers, Phys. Rev. Accel. Beams 23, 062801 (2020).

[7] Zagorodnov, I.; Dohlus, M. A semi-analytical modelling of multistage bunch com-

pression with collective effects. Phys. Rev. Accel. Beams 2011, 14, 014403

[8] S. Tomin, I.Agapov, M. Dohlus, and I. Zagorodnov, Ocelot as a framework for beam dynamics simulations of x-ray sources, in Proceedings of International Particle Accelerator Conference, Copenhagen, Denmark, 2017 (JACoW, Geneva, 2017), WEPAB031.

[9] Zagorodnov, I.; Dohlus, M.; Tomin, S. Accelerator beam dynamics at the European X-ray Free Electron Laser. Phys. Rev. Accel. Beams 2019, 22, 024401

[10] Tomin, S., Schneidmiller, E. & Decking, W. First measurement of energy diffusion in an electron beam due to quantum fluctuations in the undulator radiation. Sci Rep 13, 1605 (2023). https://doi.org/10.1038/s41598-023-28813-8

[11] B. Schmidt, S. Wesch, T. Kövener, C. Behrens, E. Hass, S. Casalbuoni, and P. Schmuueser, Longitudinal bunch diagnostics using coherent transition radiation spectroscopy, arXiv:1803.00608.

[12] M. Scholz, W. Decking, Y. Li, Beam Based Alignment in all Undulator Beamlines at European XFEL, 39th Free Electron Laser Conf, 2019, doi:10.18429/JACoW-FEL2019-THP002

[13] S. Meykopff and B. Beutner, Emittance Measurement and Optics Matching at the European XFEL, 16th Int. Conf. on Accelerator and Large Experimental Control Systems, 2017, doi:10.18429/JACoW-ICALEPCS2017-THPHA116

[14] Y. Li and J. Pflueger, Phase matching strategy for the undulator system in the European X-ray Free Electron Laser, PRAB 20, 020702 (2017)

[15] S.Tomin, G.Geloni, M.Scholz, FEL Optimization: from Model-Free to Mode-Dependent Approaches and ML prospects, 39th Free Electron Laser Conf., 2019, doi:10.18429/JACoW-FEL2019-THD03

[16] S. Tomin, L. Froehlich, M. Scholz, Status of Automated Optimization Procedures at The European XFEL Accelerator, 10th Int. Particle Accelerator Conf., 2019, doi:10.18429/JACoW-IPAC2019-TUZZPLM2

[17] S.Tomin et al, On-line Optimization of European XFEL with OCELOT, ICALEPCS'17

[18] E. L. Saldin, E. Schneidmiller, and M. V. Yurkov, The Physics of Free Electron Lasers (Springer Science & Business Media, New York, 2013), https://doi.org/ 10.1007/978-3-662-04066-9.

[19] E. Saldin, E. Schneidmiller, and M. Yurkov, On the coherent radiation of an electron bunch moving in an arc of a circle, Nucl. Instrum. Methods Phys. Res., Sect. A 398, 373 (1997).

[20] M. Borland, Y. C. Chae, P. Emma, J.W. Lewellen, V. Bharadwaj, W. M. Fawley, P. Krejcik, C. Limborg, S. V. Milton, H. D. Nuhn, R. Soliday, and M. Woodley, Start-to end simulation of self-amplified spontaneous emission free electron lasers from the gun through the undulator, Nucl. Instrum. Methods Phys. Res., Sect. A 483, 268 (2002).

[21] E. L. Saldin, E. A. Schneidmiller, and M. V. Yurkov, Longitudinal space charge-driven microbunching instability in the TESLA Test Facility linac, Nucl. Instrum. Methods Phys. Res., Sect. A 528, 355 (2004).

[22] P. Emma, J. Frisch, and P. Krejcik, A transverse rf deflecting structure for bunch length and phase diagnostic, Stanford linear accelerator center, California Technical Report No. TN-00-12, 2000.

[23] R. Lai, U. Happek, and A. J. Sievers, Measurement of the longitudinal asymmetry of a charged particle bunch from the coherent synchrotron or transition radiation spectrum, Phys. Rev. E 50, R4294 (1994).

[24] Ch. Gerth and N. M. Lockmann, Bunch Compression Monitor Based on Coherent Diffraction Radiation at European XFEL and FLASH, 10th Int. Beam Instrum. Conf., 2021, doi: 10.18429/JACoW-IBIC2021-WEPP14

[25] J. Kaiser, A. Eichler, S. Tomin and Z. Zhu, Machine Learning for Combined Scalar and Spectral Longitudinal Phase Space Reconstruction, 14th International Particle Ac-

celerator Conference, 2023, doi: 10.18429/JACoW-IPAC2023-THPL019

[26] D. P. Kingma and J. Ba, Adam: A method for stochastic optimization, 2017.

[27] I. Zagorodnov, T. Weiland, TE/TM field solver for particle beam simulations without numerical cherenkov radiation, Phys. Rev. ST Accel. Beams 8 (2005) 042001.

[28] N. Lockmann, Noninvasive Measurements of Electron Bunch Current Profiles with Few-Femtosecond Resolution at MHz Repetition Rates, PhD thesis, Hamburg 2021, doi: 10.3204/PUBDB-2021-04346.

[29] S. Tomin, W. Decking, N. Golubeva, A. Novokshonov, T. Wohlenberg, I. Zagorodnov, Longitudinal Phase Space Diagnostics With Corrugated Structure at the European XFEL, 13th International Particle Accelerator Conference, 2022, doi: 10.18429/JACoW-IPAC2022-MOPOPT020

[30] M. Hamberg, F. Brinker, M. Scholz, Commissioning and first heating with the European XFEL laser heater, 8th International Particle Accelerator Conference 494-496, 2017.

[31] J. Zhu, N. M. Lockmann, M.K. Czwalinna, H. Schlarb, Mixed Diagnostics for Longitudinal Properties of Electron Bunches in a Free-Electron Laser, Front. Phys. 10 (2022) 903559, doi: 10.3389/fphy.2022.903559